

TOWARD EMPIRICAL CONSTRAINTS ON THE GLOBAL REDSHIFTED 21 CM BRIGHTNESS TEMPERATURE DURING THE EPOCH OF REIONIZATION

JUDD D. BOWMAN¹, ALAN E. E. ROGERS², AND JACQUELINE N. HEWITT¹

Draft version October 31, 2018

ABSTRACT

Preliminary results are presented from a simple, single-antenna experiment designed to measure the all-sky radio spectrum between 100 and 200 MHz. The system used an internal comparison-switching scheme to reduce non-smooth instrumental contaminants in the measured spectrum to 75 mK. From the observations, we place an initial upper limit of 450 mK on the relative brightness temperature of the redshifted 21 cm contribution to the spectrum due to neutral hydrogen in the intergalactic medium (IGM) during the epoch of reionization, assuming a rapid transition to a fully ionized IGM at a redshift of 8. With refinement, this technique should be able to distinguish between slow and fast reionization scenarios. To constrain the duration of reionization to $\Delta z > 2$, the systematic residuals in the measured spectrum must be reduced to 3 mK.

Subject headings: Cosmology: Early Universe, Galaxies: Intergalactic Medium, Radio Lines: General

1. INTRODUCTION

The transition period at the end of the cosmic “Dark Ages” is known as the epoch of reionization (EOR). During this epoch, radiation from the very first luminous sources—early stars, galaxies, and quasars—succeeded in ionizing the neutral hydrogen gas that had filled the intergalactic medium (IGM) since the recombination event following the Big Bang. Reionization marks a significant shift in the evolution of the Universe. For the first time, gravitationally-collapsed objects exerted substantial feedback on their environments through electromagnetic radiation, initiating processes that have dominated the evolution of the visible baryonic Universe ever since. The epoch of reionization, therefore, can be considered a dividing line when the relatively simple evolution of the early Universe gave way to more complicated and more interconnected processes. Although the Dark Ages are known to end when the first luminous sources ionized the neutral hydrogen in the IGM, precisely when this transition occurred remains uncertain.

The best existing constraints on the timing of the reionization epoch come from two sources: the cosmic microwave background (CMB) anisotropy and absorption features in the spectra of high-redshift quasars. The amplitude of the observed temperature anisotropy in the CMB is affected by Thomson scattering due to electrons along the line of sight between the surface of last scattering and the detector, and thus, it is sensitive to the ionization history of the IGM through the electron column density. In addition, if there is sufficient optical depth to CMB photons due to free electrons in the IGM after reionization, some of the angular anisotropy in the unpolarized intensity can be converted to polarized anisotropy. This produces a peak in the polarization power spectrum at the angular scale size equivalent to the horizon at reionization with an amplitude pro-

portional to the optical depth (Zaldarriaga et al. 1997). Measurements by the WMAP satellite of these effects indicate that the redshift of reionization is $z_r \approx 11 \pm 4$ (Spergel et al. 2007), assuming an instantaneous transition.

Lyman- α absorption by neutral hydrogen is visible in the spectra of many high-redshift quasars and, thus, offers the second currently feasible probe of the ionization history of the IGM. Continuum emission from quasars is redshifted as it travels through the expanding Universe to the observer. Neutral hydrogen along the line of sight creates absorption features in the continuum at wavelengths corresponding to the local rest-frame wavelength of the Lyman- α line. Whereas CMB measurements place an integrated constraint on reionization, quasar absorption line studies are capable of probing the ionization history in detail along the sight-lines. There is a significant limitation to this approach, however. The Lyman- α absorption saturates at very low fractions of neutral hydrogen (of order $x_{HI} \approx 10^{-4}$). Nevertheless, results from these studies have been quite successful and show that, while the IGM is highly ionized below $z \lesssim 6$ (with typical $x_{HI} \lesssim 10^{-5}$), a significant amount of neutral hydrogen is present above, although precisely how much remains unclear (Djorgovski et al. 2001; Becker et al. 2001; Fan et al. 2002, 2003; Wyithe & Loeb 2004; Fan et al. 2006).

The existing CMB and quasar absorption measurements are somewhat contradictory. Prior to these studies, the reionization epoch was assumed generally to be quite brief, with the transition from an IGM filled with fully neutral hydrogen to an IGM filled with highly ionized hydrogen occurring very rapidly. These results, however, open the possibility that the ionization history of the IGM may be more complicated than previously believed (Haiman & Holder 2003; Cen 2003; Sokasian et al. 2003; Madau et al. 2004).

Direct observations of the 21 cm (1420 MHz) hyperfine transition line of neutral hydrogen in the IGM during the reionization epoch would resolve the existing uncertainties and reveal the evolving properties of

Electronic address: jdbowman@mit.edu

¹Massachusetts Institute of Technology, Kavli Institute for Astrophysics and Space Research, Cambridge, Massachusetts, USA

²Massachusetts Institute of Technology, Haystack Observatory, Westford, Massachusetts, USA

the IGM. The redshifted 21 cm signal should appear as a faint, diffuse background in radio frequencies below $\nu < 200$ MHz for redshifts above $z > 6$ (according to $\nu = 1420/[1+z]$ MHz). For diffuse gas in the high-redshift ($z \approx 10$) IGM, the expected unpolarized differential brightness temperature of the redshifted 21 cm line relative to the pervasive CMB is readily calculable from basic principles and is given by (Zaldarriaga et al. 2004, their § 2)

$$\delta T_{21}(\vec{\theta}, z) \approx 23 (1 + \delta) x_{HI} \left(1 - \frac{T_\gamma}{T_S}\right) \times \left(\frac{\Omega_b h^2}{0.02}\right) \left[\left(\frac{0.15}{\Omega_m h^2}\right) \left(\frac{1+z}{10}\right)\right]^{1/2} \text{ mK}, \quad (1)$$

where $\delta(\vec{\theta}, z)$ is the local matter over-density, $x_{HI}(\vec{\theta}, z)$ is the neutral fraction of hydrogen in the IGM, $T_\gamma(z) = 2.73 (1+z)$ K is the temperature of CMB at the redshift of interest, $T_S(\vec{\theta}, z)$ is the spin temperature that describes the relative population of the ground and excited states of the hyperfine transition, and Ω_b is the baryon density relative to the critical density, Ω_m is the total matter density, and h specifies the Hubble constant according to $H_0 = 100 h \text{ km s}^{-1} \text{ Mpc}^{-1}$. From Equation 1, we see that perturbations in the local density, spin temperature, and neutral fraction of hydrogen in the IGM would all be revealed as fluctuations in the brightness temperature of the observed redshifted 21 cm line.

The differential brightness temperature of the redshifted 21 cm line is very sensitive to the HI spin temperature. When the spin temperature is greater than the CMB temperature, the line is visible in emission. For $T_S \gg T_\gamma$, the magnitude of the emission saturates to a maximum (redshift-dependent) brightness temperature that is about 25 to 35 mK for a mean-density, fully neutral IGM between redshifts 6 and 15, assuming a Λ CDM cosmology with $\Omega_m = 0.3$, $\Omega_\Lambda = 0.7$, $\Omega_b = 0.04$, and $h = 0.7$. At the other extreme, when the spin temperature is very small and $T_S \ll T_\gamma$, the line is visible in absorption against the CMB with a potentially very large (and negative) relative brightness temperature.

A number of factors are involved in predicting the typical differential brightness temperature of the redshifted 21 cm line as a function of redshift. In particular, the spin temperature must be treated in detail, including collisional coupling between the spin and kinetic temperatures of the gas, absorption of CMB photons, and heating by ultra-violet radiation from the first luminous sources. We direct the reader to Furlanetto et al. (2006) for a good introduction to the topic. The results of several efforts to predict the evolution of the differential brightness temperature of the redshifted 21 cm line have yielded predictions that are generally consistent in overall behavior, but vary highly in specific details (Madau et al. 1997; Shaver et al. 1999; Gnedin & Shaver 2004; Furlanetto 2006). These models tend to agree that, for a finite period at sufficiently high redshifts ($z \gtrsim 20$), the HI hyperfine line should be seen in absorption against the CMB, with relative brightness temperatures of up to $|\delta T_b| \lesssim 100$ mK. This is because the IGM initially cools more rapidly than the CMB following recombination (Shapiro et al. 1994; Madau et al. 1997). During this period, fluctuations in the differential brightness temperature of the redshifted 21 cm

background should track the underlying baryonic matter density perturbations (Sunyaev & Zeldovich 1972; Hogan & Rees 1979; Scott & Rees 1990; Iliev et al. 2002, 2003; Loeb & Zaldarriaga 2004; Barkana & Loeb 2005). Eventually, however, the models indicate that the radiation from the first generations of luminous sources will elevate the spin temperature of neutral hydrogen in the IGM above the CMB temperature and the redshifted 21 cm line should be detected in emission with relative brightness temperatures up to the expected maximum values (of order 25 mK). Finally, during the reionization epoch, the neutral hydrogen becomes ionized, leaving little or no gas to produce the HI emission, and the apparent differential brightness temperature of the redshifted 21 cm line falls to zero as reionization progresses. As the gas is ionized, a unique pattern should be imprinted in the redshifted 21 cm signal that reflects the processes responsible for the ionizing photons and that evolves with redshift as reionization progresses (Madau et al. 1997; Tozzi et al. 2000; Ciardi & Madau 2003; Zaldarriaga et al. 2004; Furlanetto et al. 2004). The details of the specific timing, duration, and magnitude of these features remains highly variable between theoretical models due largely to uncertainties about the properties of the first luminous sources.

Measuring the brightness temperature of the redshifted 21 cm background could yield information about both the global and the local properties of the IGM. Determining the average brightness temperature over a large solid angle as a function of redshift would eliminate any dependence on local density and temperature perturbations and constrain the evolution of the product $\bar{x}_{HI}(1 - T_\gamma/T_S)$, where we use the bar to denote a spatial average. During the reionization epoch, it is, in general, believed to be a good approximation to assume that $T_S \gg T_\gamma$ and, therefore, that the brightness temperature is proportional directly to \bar{x}_{HI} . Global constraints on the brightness temperature of the redshifted 21 cm line during the EOR, therefore, would directly constrain the neutral fraction of hydrogen in the IGM. Such constraints would provide a basic foundation for understanding the astrophysics of reionization by setting bounds on the duration of the epoch, as well as identifying unique features in the ionization history (for example if reionization occurred in two phases or all at once). They would also yield improvements in estimates of the optical depth to CMB photons and, thus, would help to break existing degeneracies in CMB measurements between the optical depth and properties of the primordial matter density power spectrum (Tegmark et al. 2006). For these reasons, several efforts are underway to make precise measurements of the radio spectrum below $\nu < 200$ MHz ($z > 6$). In this paper, we report on the initial results of the Experiment to Detect the Global EOR Signature (EDGES). In § 2, we describe the specific approach used for EDGES to address the issue of separating the redshifted 21 signal from the foreground emission. We then give an overview of the EDGES system in § 3, followed by the results of the first observing campaign with the system in § 4, along with a discussion of the implications for future single-antenna measurements.

2. METHOD

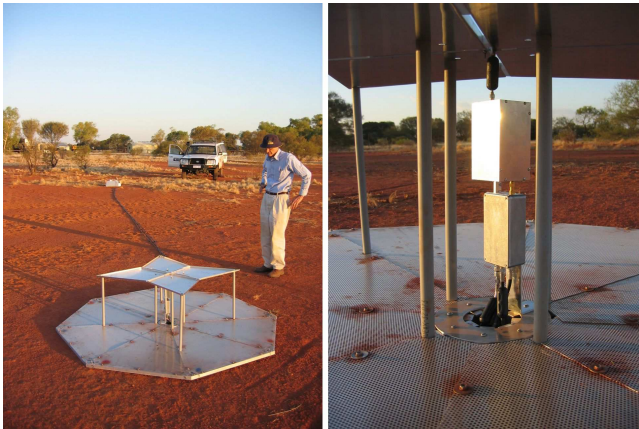


FIG. 1.— EDGES deployed at Mileura Station in Western Australia. The left panel shows the full antenna and ground screen in the foreground and the analog-to-digital conversion and data acquisition module in the background. The right panel is a close-up view of the amplifier and switching module connected directly to the antenna (through the balun).

In principle, the global brightness temperature measurement is much less complicated to perform than the detection of local perturbations in the redshifted 21 cm background (which will be attempted in the near future by the Mileura Widefield Array [MWA], Low Frequency Array [LOFAR], Giant Metrewave Radio Telescope [GMRT], and Twenty-one Centimeter Array [21CMA]). Since the desired signal for the global measurement is the mean brightness temperature due to redshifted 21 cm emission (or absorption) over the entire sky, there is no need for high angular resolution or imaging. A single antenna tuned to the appropriate frequencies could reach the required sensitivity (~ 25 mK) within only one hour of integration time, assuming a reasonable spectral resolution of ~ 1 MHz (equivalent to $\Delta z \approx 0.1$ at $z \approx 8$). There is a fundamental complication with such an experiment, however, arising from the global nature of the signal. Since the expected redshifted 21 cm emission fills the entire sky, there is no ability to perform comparison switching between the target field and a blank field. The problem this causes is two-fold. First, it is difficult to separate the contribution to the measured spectrum due to the redshifted HI signal from that of any other all-sky emission, including Galactic synchrotron and free-free radiation, the integrated contribution of extragalactic continuum sources, or the CMB. Second, for similar reasons, it is difficult to avoid confusing any systematic effects in the measured spectrum due to the instrument or environment with received signal from the sky. The severity of these problems is exacerbated in single-antenna measurements by the intensity of the Galactic synchrotron emission. Unlike interferometric observations, a single antenna is sensitive to the large-scale emission from the Galaxy, providing a 200 to 10,000 K foreground in the measured spectrum.

Determining the ~ 25 mK redshifted 21 cm contribution to the radio spectrum requires separating the signal from the foreground spectrum at better than 1 part in 10,000. This can be accomplished by taking advantage of the differences between the spectra of the Galactic and extragalactic foregrounds and the anticipated redshifted 21 cm contribution. As discussed by Shaver et al. (1999), Galactic synchrotron emission is the

dominate component of the astrophysical foregrounds below $\nu < 200$ MHz, accounting for all but approximately 30 to 70 K of the foregrounds at 178 MHz (Bridle 1967). Its spectrum is very nearly a power-law given, in temperature units, by $T_{gal}(\nu) \sim \nu^{-\beta}$, where $\beta \approx 2.5$ is the spectral index. The spectral index is generally constant over the frequencies of interest ($50 \lesssim \nu \lesssim 200$ MHz), although it is known to flatten with decreasing frequency due to self-absorption. The intensity of the synchrotron emission and the exact value of the spectral index depend on Galactic coordinate. The amplitude varies over an order of magnitude, between about $200 < T_{gal} < 10,000$ K at 150 MHz (peaking toward the Galactic center and along the Galactic plane), while the spectral index has small variations of order $\sigma_{\beta} \approx 0.1$ dependent largely on Galactic latitude, with the steepest regions occurring at high Galactic latitudes. Free-free emission in the Galaxy and discrete Galactic and extragalactic continuum sources also have spectra that can be reasonably described by power-laws. The integrated flux from extragalactic continuum sources is generally isotropic on large scales and accounts for the majority of the remaining power in the low-frequency radio spectrum, with free-free emission making up only about 1% of the total power. The combined spectrum due to the astrophysical foregrounds is smooth and remains similar to a power-law profile.

On the other hand, as the apparent differential brightness temperature of the redshifted 21 cm background transitions from $T_{21} = 0$ mK at very high redshift to $T_{21} \approx -100$ mK before heating of the IGM by the first luminous sources, and then climbs to $T_{21} \approx 25$ mK at the beginning of the reionization epoch before falling back to $T_{21} \approx 0$ mK at the end of reionization, the global mean redshifted 21 cm spectrum may contain up to three relatively sharp features between $50 \lesssim \nu \lesssim 200$ MHz that would not be represented well by a power-law profile. For the large solid angles of a single antenna beam, the mean redshifted 21 cm signal should vary little from one location to another on the sky. Furlanetto (2006) and Gnedin & Shaver (2004) have calculated example global mean redshifted 21 cm spectra for various assumptions of stellar formation histories.

The specific approach employed with EDGES to exploit these expected differences in spectral characteristics in order to overcome the difficulty in separating the foreground and signal contributions in the measured spectrum is to limit the scope of the experiment to test for discontinuous features in the spectrum, since these would necessarily be due to the rapid transitions in the redshifted 21 cm brightness temperature and not the spectrally smooth foregrounds. In particular, the frequency response of the system is designed to test for fast reionization only (and not the transitions that might arise at higher redshifts from cooling and heating of the IGM). In the extreme case that the transition from a fully neutral to a fully ionized IGM was virtually instantaneous, such that $\bar{x}_{HI}(z_r) \rightarrow \infty$, where z_r is the redshift of reionization, the contribution to the global spectrum at the frequencies corresponding to the reionization epoch would approach a step function. A sharp feature resembling a step function that is superimposed on the smooth power-law-like foreground spectrum should be relatively easy to identify. And if reionization were to progress more

slowly, producing a smooth transition that spanned a large range of redshifts and many tens of MHz, a simple model could be used to set limits on the maximum rate of the transition.

In principle, a variety of such models could be devised to use in tests for the presence of a step feature in the radio spectrum due to a rapid reionization. A simple low-order polynomial fit to the measured spectrum would reveal such a discontinuous feature in the residual spectrum after subtracting the fit and, thus, would be able to determine the redshift range of a rapid reionization. Figure 2 illustrates this approach by plotting a model (described in Section 4.1) of the redshifted 21 cm contribution to the measured spectrum along with the residuals after a seventh-order polynomial fit is removed from a simulated sky spectrum. This is the method used for the preliminary EDGES measurements. An advantage of this approach for global reionization experiments is that, given sufficient sensitivity, even a null result could still constrain $\hat{x}_{HI}(z)$ and, thereby, distinguish between slow and fast reionization scenarios.

3. EXPERIMENT DESIGN

By focusing (at least initially) on confirming or ruling out a fast reionization scenario, the design of the EDGES system is able to be relatively simple. The primary need is to reduce any instrumental or systematic contributions to the measured power spectrum that vary rapidly with frequency, since these could be confused with a sharp feature in the spectrum due to a fast reionization of the IGM. Such contributions could be due to terrestrial transmitters, reflections of receiver noise or sky noise from nearby objects, undesirable resonances within the electronics or the radio-frequency interference (RFI) enclosures, or spurious signals introduced by the digital sampling system. In this section, we provide an overview of the experimental design and setup, highlighting aspects that are relevant to reducing the effects of both the external and internal sources of systematic errors. Additional details on the analysis of systematic contributions and the hardware design can be found in the EDGES memorandum series³.

3.1. Site Selection

Some of the contributions to the systematic uncertainty listed above can be addressed by careful selection of the observing site. Avoiding terrestrial transmitters (primarily from FM radio and television stations) is the most serious problem. Even at distances of hundreds or thousands of kilometers, tropospheric ducting and scattering (troposcatter), sporadic E propagation in the ionosphere, and reflections from meteors are all capable of transferring a significant amount of power from Earth-based transmitters. The background produced by the integrated effect of many distant transmitters may have significant spectral structure above the expected redshifted 21 cm level. For example, a single, 100 kW FM radio station at 300 km from the observing site could produce up to a 100 K effective temperature in a 1 MHz channel due to troposcatter, or 100 mK due to meteor reflections. Fortunately, these mechanisms of atmospheric propagation exhibit diurnal or transient behavior (as is

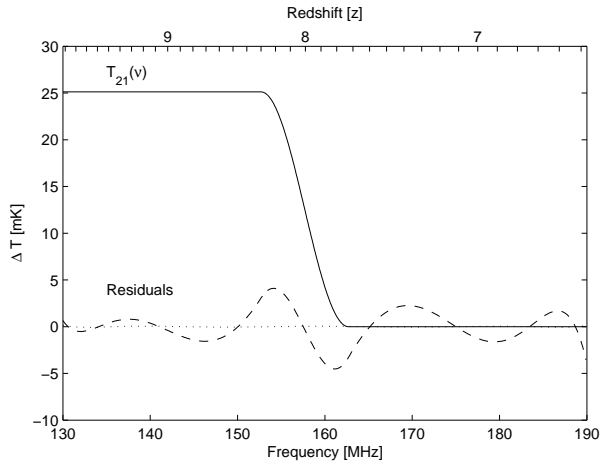


FIG. 2.— Example of redshifted 21 cm contribution (solid) to T_{sky} based on the model described in § 4.1 with $\Delta T_{21} = 25$ mK, $z_r = 8$, and $\Delta z = 0.6$. The residuals are also shown for a seventh-order polynomial fit to a simulated spectrum between 130 and 190 MHz with (dash) and without (dot) the redshifted 21 cm contribution. The foreground contribution was modeled for the plot using $\beta = 2.5$, and $T_{gal}(150 \text{ MHz}) = 250$ K.

the case for sporadic E propagation, tropospheric ducting, and meteor reflections) or require specific geometries for peak efficiency (as is the case for troposcatter), making sensitive measurements possible at remote sites at least some of the time.

Another concern is that local objects in the environment will scatter both external noise and receiver noise, which will then be picked up by the system and correlate with the original noise, causing sinusoidal ripples in the measured spectrum. We have estimated the magnitude of the reflections of the Galactic foreground from objects like trees and mountains on the horizon where the antenna gain is reduced by a factor of 20 dB or more. As long as objects subtend solid angles under about 100 deg^2 , the spectrum will only be affected by a few parts per million (*ppm*). We have also considered the magnitude of noise originating from the receiver that will be returned by a nearby scatterer. Even if we assume that this noise is perfectly correlated with the internal receiver noise, it will only produce ripples in the spectrum at the level of a few *ppm* provided that the object, like a tree subtending a few deg^2 , is more than ~ 100 m away or a larger object, subtending $\sim 100 \text{ deg}^2$ is more than ~ 1 km away.

Reflections of signals from compact radio sources may also be correlated. In this case the scatterer and the receiving antenna act like an adding interferometer to produce ripples in the spectrum. However, these effects are extremely small since a 1 Jy source results in under 1 mK of antenna temperature for the dipole-based EDGES system and the reflected signal is much smaller still. The ground reflection has been eliminated by placing the antenna on the ground. A brief discussion on the impact of these effects in radio astronomy measurements can be found also in Rohlfs & Wilson (1996).

3.2. Hardware Configuration

Following a careful choice of the deployment site for the experiment, the remaining sources of systematic uncertainty result from the hardware design of the system.

³ <http://www.haystack.mit.edu/ast/arrays/Edges/>

The EDGES system consists of three primary modules: 1) an antenna, 2) an amplifier and comparison switching module, and 3) an analog-to-digital conversion and storage unit. The antenna, shown in Figure 1, is a “fat” dipole-based design derived from the four-point antenna of Suh et al. (2003, 2004). The design was chosen for its simplicity and its relatively broad frequency response that spans approximately an octave. The response of the antenna was tuned to 100 to 200 MHz by careful selection of the dipole dimensions. In order to eliminate reflections from the ground and to reduce gain toward the horizon, the antenna is placed over a conducting mesh that rests directly on the ground. The mesh is constructed from thin, perforated metal sheets to reduce weight and is shaped to match an octagonal support structure below the ground screen. The diameter of this ground screen is approximately 2 m.

Although the antenna is constructed with perpendicular dipoles capable of receiving dual linear polarizations, only one polarization of the crossed-dipole is sampled by the receiver in order to reduce the cost of the system. This is acceptable since the spatially averaged all-sky spectrum is expected to have essentially no polarized component. The Galactic foreground does exhibit strong polarization in certain regions, such as the “fan region” around $\ell \approx 140^\circ$, $b \approx 8^\circ$, which has an extended polarized component of about 3 K (Wilkinson 1973). Such a region could produce a ripple in the measured spectrum from a single linear polarization as the polarization angle rotates with frequency. Under the worst circumstances, if such a region were located at the peak of the EDGES beam, the magnitude of the ripple could reach ~ 50 mK. Away from the Galactic plane, however, where EDGES observations are generally targeted in order to reduce the system temperature, it is more likely that the effects of polarization would be at least an order of magnitude lower. Furthermore, if the rotation measure (RM) is of order 10 rad m^{-2} , then the polarized component could be averaged out over ~ 1 MHz. Nevertheless, in future versions of EDGES, both ports of the antenna will be sampled in order to check for polarization effects and other systematic effects that result from the non-uniformity of Galactic radiation.

A dipole antenna is naturally a balanced electrical system. To convert from the balanced antenna leads to the unbalanced receiver system (in which one lead is grounded), a short coaxial cable enclosed in a clamp-on split ferrite core with a high impedance is used as a common-mode choke balun⁴ and is connected directly to the terminals of the antenna with the central conductor fastened to one element and the braided shielding to the other.

The amplifier module consists of two stages that are contained in separate aluminum enclosures to reduce coupling between the low-noise amplifiers. Each stage provides 33 dB of gain for a total of 66 dB. Bandpass filtering of the signal is also performed in the second stage, and the resulting half-power bandwidth spans approximately

50 to 330 MHz. The amplifier chain can be connected through a voltage controlled three-position switch to one of three inputs: the antenna, an ambient load, or an ambient load plus a calibration noise source. Switching between the ambient load and the antenna provides a comparison to subtract spurious instrumental signals in the measured sky spectrum.

Impedance mismatch between the antenna and the amplifiers causes reflections of the sky noise within the electrical path of the instrument that produce an undesirable sinusoidal ripple in the measured spectrum due to the frequency-dependence of the phase of the reflections at the input to the amplifier. To reduce the effects of these reflections in EOR measurements, the input to the amplifier chain is connected directly to the balun on the antenna (with no intermediate transmission cable), as shown in Figure 1. While absolute calibration is limited in this configuration by the effect of the unknown phases of the reflections on the measured spectrum, the compact size of the antenna and the small signal path delays result in a smooth spectral response.

The amplifier module is connected to the analog-to-digital conversion module by three low-loss coaxial transmission cables. The cables provide power, switching control, and signal transmission, respectively. Common-mode current on these cables (i.e. current that is on the outer surface of the shielding in the coaxial cable, or current that is unidirectional on both the central conductor and inner surface of the shielding) is also capable of producing reflections and additional sinusoidal ripples in the measured spectrum. The ferrite core balun used between the antenna and amplifiers allows common-mode current of approximately 10% of the differential mode. Although most of this current is transferred to the ground screen by direct contact between the amplifier module casing and the ground screen, some current persists and leaks through the casing of the amplifier module and onto the shielding of the three cables connecting the amplification module to the analog-to-digital conversion module. To reduce this current to less than 0.005% of the differential mode current, additional clamp-on ferrite cores are placed every meter on the transmission cables.

Finally, the analog-to-digital conversion is accomplished with an Acqiris AC240⁵ 8-bit digitizer with maximum dynamic range of 48 dB (although, in practice, the effective dynamic range was substantially lower due to coupling between the digital output of the converter and its input). The AC240 uses an embedded field programmable gate array (FPGA) to perform onboard Fast Fourier Transform (FFT) and integration of the power spectrum in realtime. The spectrometer is clocked at 1 GS/s and the Fourier transform processes 16,384 channels, giving a bandwidth of 500 MHz and a raw spectral resolution of about 30 kHz. The broadband spectrometer employs the FPGA code of Benz et al. (2005) and a Blackman-Harris window function is used to improve the isolation between neighboring frequency channels at the expense of reducing the effective spectral resolution to 122 kHz. The unit is contained on a CompactPCI card connected to a host computer. The digitizer and host computer, along with a power transformer and interface

⁴ This balun provides a 1:1 impedance transition and operates on the same principle as the quarter wavelength sleeve balun described by Kraus (1988, page 742). The ferrite provides a high impedance over a wide frequency range to reduce the common-mode currents, whereas the sleeve balun provides a high impedance over only a limited frequency range close to the quarter wavelength resonance.

⁵ <http://www.acqiris.com/products/analyzers/cpci-signal-analyzers/ac240-platform.html>

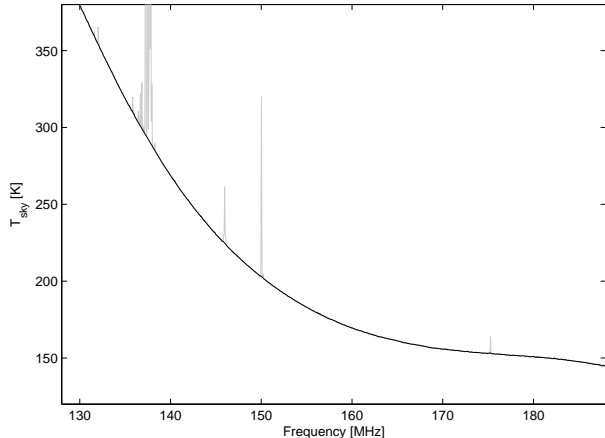


FIG. 3.— Integrated spectrum used for upper limit analysis of reionization signal. The sky temperature, T_{sky} , is an estimate based on modeled values for cable losses and no correction for antenna reflections. The spectrum represents the best 10% of the data from observations over two nights. It is selected by discarding individual observation cycles (see § 3.3) containing periods of particularly intense radio frequency interference. A total of approximately 1.5 h of integration is included (3.75 h including the ambient load and calibrator noise source measurements in each cycle). The black curve shows the spectrum after de-weighting the interferers (shown in gray) present in the retained observations.

circuitry for controlling the amplifier module with the serial port of the computer, are enclosed in an aluminum box to prevent self interference.

3.3. The Measured Spectrum

The measured spectra from each of the three switch positions can be combined to produce a calibrated estimate of the true sky spectrum. The three spectra are given by

$$\begin{aligned} p_0 &= g (T_L + T_R) (1 + n_0) \\ p_1 &= g (T_L + T_R + T_{cal}) (1 + n_1) \\ p_2 &= g (T_A + T_R) (1 + n_2) \end{aligned} \quad (2)$$

where the explicit frequency dependence of each term has been dropped and p_0 is the spectrum for the ambient load, p_1 is the spectrum for the ambient load plus calibration noise, and p_2 is the spectrum for the antenna. In this terminology, g is the gain, T_L is the ambient load temperature, T_R is the receiver noise temperature, T_{cal} is the calibration noise temperature, and T_A is the antenna temperature. Thermal uncertainty in the measurements is explicitly included in the Gaussian random variables n_0 , n_1 , and n_2 , the magnitudes of which are given by $n_i = (\epsilon b \tau_i)^{-1/2}$, where $\epsilon = 0.5$ is the efficiency for the Blackman-Harris window function (which could be improved to 0.93 by processing two sets of overlapping windows), $b = 122 \times 10^3$ Hz is the resolution bandwidth, and τ_i is the integration time in seconds (for each switch position, i). Temporarily setting the noise terms to zero, $n_i \rightarrow 0$, and solving for the antenna temperature yields

$$T_A = T_{cal} \frac{p_2 - p_0}{p_1 - p_0} + T_L. \quad (3)$$

In practice, the impedance match between the antenna and receiver is not perfect and some of the incident sky noise may be reflected back out of the system. This

produces deviations between the derived sky temperature found using Equation 3 and the true sky spectrum. Independent measurements of the impedance mismatch can be used to correct these deviations by applying a frequency-dependent multiplicative factor to T_A that is proportional to the inverse of the reflection coefficient. For the EDGES system, this correction was measured by two methods: we used a network analyzer in the laboratory to determine the impedance of the antenna, and we reconfigured the system in the field with a long cable inserted between the antenna and amplifier module so that reflections between the two elements were visible in the measured spectrum and could be used to calibrate the reflection coefficient. In both sets of measurements, the corrections were found to be small (of order 1%) and smooth (able to be fit by a low-order polynomial in frequency) over the band of interest. For the remainder of this paper, we will ignore this correction since its effects are easily absorbed by the polynomial fit technique used to constrain the redshifted 21 cm contribution to the spectrum.

Adding the noise terms back in and solving in the limit that $T_{cal} \gg (T_L \approx T_A) > T_R$ results in an estimate of the thermal uncertainty per frequency channel of approximately

$$\Delta T_{A,rms} \approx \sqrt{n_0^2(T_L + T_R)^2 + n_1^2(T_L)^2 + n_2^2(T_A + T_R)^2}. \quad (4)$$

For optimal efficiency, the three terms contributing to $\Delta T_{A,rms}$ should be comparable in magnitude. Substituting $T_L = 300$ K, $T_A = 250$ K and $T_R = 20$ K, we find that the terms are comparable as long as approximately equal time is spent in each switch position. In addition, a 1 hour integration in each switch position (3 hours total) will result in a thermal uncertainty in the estimate of the antenna temperature of $\Delta T_{A,rms} \approx 35$ mK within each 122 kHz frequency channel.

To acquire a series of estimates of the true sky spectrum using this technique, software on the host computer cycles the amplifier module between the three switch positions and triggers the digitizer to acquire, Fourier transform, and accumulate data for a predefined duration at each of the switch positions. The integration durations per switch position are $\tau_{\{0,1,2\}} = \{10, 5, 10\}$ seconds for the ambient load, ambient load plus calibration noise source, and antenna, respectively, giving a duty cycle of about 40% on the antenna. This loop is repeated approximately every 25 seconds for the duration of the observations and the resulting measurements are recorded to disk.

4. INITIAL RESULTS

The EDGES system was deployed at the radio-quiet Mileura Station in Western Australia from 29 November through 8 December 2006. These dates were chosen such that the Galactic center would be below the horizon during most of the night, keeping the system temperature as low as possible for the measurements. The system was located approximately 100 m from the nearest buildings in a clearing with no nearby objects and no obstructions above $\sim 5^\circ$ on the horizon, and the antenna was aligned in an approximately north-south/east-west configuration. The system was operated on 8 consecutive nights during the deployment, with 5 of the nights

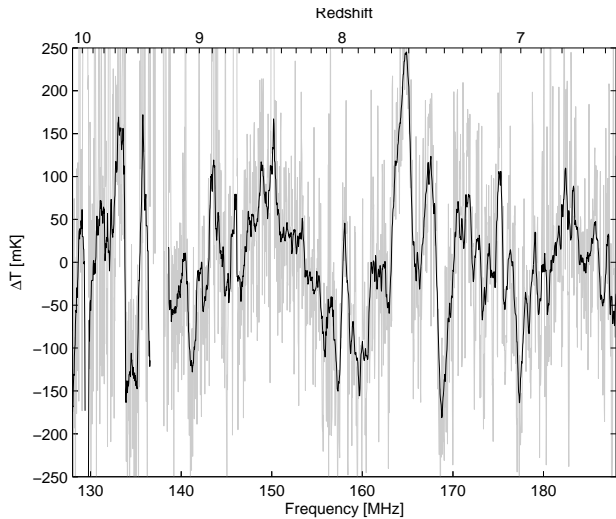


FIG. 4.— Residuals after subtraction of seventh-order polynomial fit to measured spectrum shown in Figure 3. The gray line is the raw spectrum with 122 kHz resolution. The black line is after smoothing to 2.5 MHz resolution to reduce the thermal noise to below the systematic noise. The rms of the smoothed fluctuations is approximately 75 mK (see Figure 5).

dedicated to EOR observing. In total, over 30 h of relevant drift scans were obtained, but strong, intermittent interference from satellites complicated the measurements and only approximately 8 h of high-quality observations were retained as the primary data set. Although the satellite interferers that complicated the measurements were narrow-band and, in many cases, were easily removed through excision of the effected spectral channels, the limited dynamic range of the EDGES system resulted in clipping of the analog-to-digital converter and corruption of the full band during especially strong transmissions. This required all channels to be omitted from the data set in those instances. In particular, it was found that the low Earth orbiting satellites of Orbcomm (transmitting between approximately 136 and 138 MHz), as well as satellite beacons (at 150 MHz) from discarded spacecraft were particularly troublesome. The Orbcomm activity was somewhat variable and usually decreased during the night. The typical duration of a pass was approximately 15 minutes, during which time the power in the satellite signal could easily reach an order of magnitude greater than the integrated sky noise over the band. While previous observations at the site with prototype MWA equipment (Bowman et al. 2007) have demonstrated (in a subset of the full target band) that it is possible to reach the sensitivities required for EDGES despite the satellites and other sources of interference, improvements to the EDGES digitizing system, such as an upgrade of the analog-to-digital converter to 10 or 12 bits, would certainly help to alleviate the difficulties encountered during this observing campaign and increase the usable fraction of measurements.

From the primary data set remaining after transient RFI exclusion, a stringent filter was applied to select the best 1.5 h of sky-time when transient interference signals were weakest. The final cut of data included measurements from multiple nights and spanned a range of local apparent sidereal time (LST) between 0 and 5 h. The sky temperature at 150 MHz derived from the system during

this period was found to have a minimum of ~ 240 K at about 3 h LST and a maximum of ~ 280 K at 5 h LST. The integrated spectrum generated from these measurements is shown in Figure 3. Frequency channels containing RFI were identified in the integrated spectrum by an algorithm that employs a sliding local second-order polynomial fit and iteratively removes channels with large errors until the fit converges. The affected channels were then weighted to zero in subsequent analysis steps. To look for small deviations from the smooth foreground spectrum, a seventh-order polynomial was fit to the measured spectrum between 130 and 190 MHz (where the impedance match between the antenna and receiver was nearly ideal) and subtracted.

The residual deviations in the measured sky spectrum after the polynomial fit and subtraction are shown in Figure 4. The rms level of systematic contributions to the measured spectrum was found to be $\Delta T_{rms} \approx 75$ mK, a factor of ~ 3 larger than the maximum expected redshifted 21 cm feature that would result from a rapid reionization. Although it is not obvious in Figure 4, the variations in the residuals are due to instrumental contributions and not thermal noise. The large variations between 163 and 170 MHz are due to the 166 MHz PCI-bus clock of the AC240 and computer, while the gap centered at approximately 137 MHz is due to RFI excision of the Orbcomm satellite transmissions over a region spanning more than 2.5 MHz. Analysis of the dependence of ΔT_{rms} on integration duration is shown in Figure 5 and illustrates that the rms of the residuals follows a thermal profile $\sim (b\tau)^{-1/2}$ initially and then saturates to a constant value. After smoothing to 2.5 MHz resolution ($\Delta z \approx 0.2$), the instrumentally dominated 75 mK threshold is reached in approximately 20 minutes (1200 s) of integration on the sky (50 minutes of total integration in all three switch positions). Reordering the individual 25-second observation cycles used in the full integration does not change the behavior in Figure 5, and longer integrations (up to approximately 3 h of sky time), using observation cycles with more intense interference, continued to decrease the thermal noise, but leave the spurious signals and systematic effects unchanged.

4.1. Limits on Reionization History

Although the sensitivity level of the initial observations with the EDGES system was limited by instrumental effects in the measured spectrum at a level greater than the expected maximum contribution due to redshifted 21 cm emission, weak constraints can still be placed on the reionization history. In addition, it is possible to make a quantitative assessment of how much improvement must be made before significant constraints are possible, as well as to characterize the best-case outcome of future efforts using similar approaches. To begin, we introduce a model for the sky spectrum such that

$$T_{sky}(\nu) = T_{gal}(\nu) + T_{cmb} + T_{21}(\nu) \quad (5)$$

where T_{gal} represents the contribution of all the foregrounds (and is dominated by the Galactic synchrotron radiation), $T_{cmb} = 2.73$ K is the CMB contribution, and T_{21} is the specific form for the frequency-dependence of the redshifted 21 cm emission during the transition from the fully neutral to fully ionized IGM. This model neglects any directional or temporal variation in T_{sky} and,

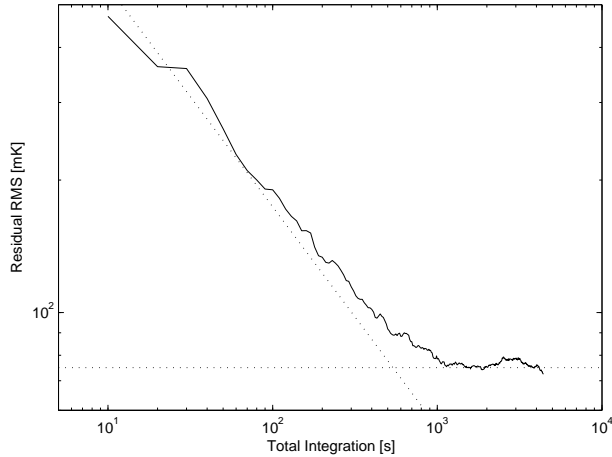


FIG. 5.— Characteristic amplitude of the residuals to the polynomial fit as a function of integration time on the sky. The *rms* follows a thermal $(b\tau)^{-1/2}$ dependency until saturating at a constant 75 mK noise level due to the instrumental errors introduced into the measured spectrum. The dotted lines are guides for the eye showing a $(b\tau)^{-1/2}$ profile and a constant 75 mK contribution.

therefore, implicitly assumes an angular average over the antenna beam and a time average over the drift scan measurements performed for the experiment. Since T_{cmb} and T_{21} are taken to be constant over the sky, only the T_{gal} contribution is affected by this simplification. This does not impact the result, however, as long as the foreground emission varies slowly on the sky and the antenna pattern changes slowly with frequency—conditions that are presumed to be met in the high Galactic latitude region sampled by the dipole-based EDGES system. As a test of this assumption, we calculated the residuals after the polynomial fit for a bright source with flux comparable to Cas A (1400 Jy at 100 MHz) and spectral index $\beta = 2.77$ at various positions in the antenna beam using simulated beam patterns to determine the frequency-dependence. We found, in all cases, less than a $\sim 50 \mu\text{K}$ residual.

During the reionization epoch, we define T_{21} to be given by

$$T_{21}(z) = \Delta T_{21} \frac{1}{2} \left\{ 1 + \cos \left[\frac{\pi(z_r - z - \Delta z/2)}{\Delta z} \right] \right\}, \quad (6)$$

where ΔT_{21} is constant and is the maximum amplitude of the redshifted 21 cm contribution, z_r is the redshift when $\bar{x}_{HI}(z_r) = 0.5$, Δz is the total duration of the reionization epoch, and we use $\nu = 1420/(1+z)$ MHz to convert back to frequency units. Before the reionization epoch ($z > z_r + \Delta z/2$), $T_{21} \equiv \Delta T_{21}$, while after reionization ($z < z_r - \Delta z/2$), $T_{21} \equiv 0$. The exact form of the transition used for T_{21} has little influence on the outcome of the constraints as long as it is reasonably smooth. Figure 2 illustrates the modelled redshifted 21 cm spectrum. The free parameters in the model are z_r , Δz , and ΔT_{21} .

For the EDGES best-response frequency range, a center redshift around $z_r = 8$ allows the largest range of Δz to be explored. By simulating the combined sky spectrum, T_{sky} , for a range of the two remaining free parameters, we can determine the *rms* of the residuals that would remain following the polynomial fit used in the EDGES data analysis. Comparing the *rms* of the

residuals in the models to the 75 mK *rms* of the initial measurements gives a good estimate of the region of parameter space ruled out so far. Figure 6 illustrates the results of this process. The line defining the ruled-out region is computed by finding the locus of parameters that make the *rms* residuals in the model equal to 75 mK. While a more statistically robust analysis is clearly possible, little benefit would be gained for the initial measurements presented here due to the severe systematic effects present in the spectrum.

From Figure 6, it is clear that the initial results constrain only a small portion of parameter space that is well outside the expected region for both the intensity of the redshifted 21 cm signal and the duration of reionization. The best constraint, in the case of a nearly instantaneous reionization, is that the redshifted 21 cm contribution to the spectrum is not greater than about $\Delta T_{21} \lesssim 450$ mK before the transition. Reducing the systematic contributions in the measured spectrum by more than an order of magnitude to $\Delta T_{rms} < 7.5$ mK would begin to allow meaningful constraints, while an improvement of a factor of 25 to $\Delta T_{rms} \approx 3$ mK would be able to rule out a significant portion of the viable parameter range and constrain $\Delta z > 2$. In principle, such an improvement is possible with minor modifications to the EDGES system. Reaching a systematic uncertainty below ~ 3 mK, however, is likely to be infeasible without a redesign of the experimental approach because errors in the polynomial fit to the overall power-law-like shape of the sky spectrum, $T_{sky}(\nu)$, are the dominant source of uncertainty below that level in the current approach. The sharp cut-off at $\Delta z \approx 2$ in parameter space is the result of using a seventh-order polynomial to fit a 60 MHz bandwidth, thus yielding a maximum residual scale size of order 10 MHz, which corresponds to $\Delta z \approx 2$ at $z \approx 8$. If the same polynomial could be reasonably fit to a larger bandwidth (or a lower-order polynomial fit to the existing bandwidth), then Δz could be probed to larger values.

5. CONCLUSION

In principle, useful measurements of the redshifted 21 cm background can be carried out with a small radio telescope. These measurements would be fundamental to understanding the evolution of the IGM and the EOR. In particular, the global evolution of the mean spin temperature and mean ionization fraction of neutral hydrogen in the high redshift IGM could be constrained by very compact instruments employing individual radio antennas. We have reported preliminary results to probe the reionization epoch based on this approach from the first observing campaign with the EDGES system. These observations were limited by systematic effects that were an order of magnitude larger than the anticipated signal and, thus, ruled out only an already unlikely range of parameter space for the differential amplitude of the redshifted 21 cm brightness temperature and for the duration of reionization. Nevertheless, the results of this experiment indicate the viability of the simple global spectrum approach.

Building on the experiences of these initial efforts, modifications to the EDGES system are underway to reduce the residual systematic contribution in the measured spectrum and to expand the frequency coverage of

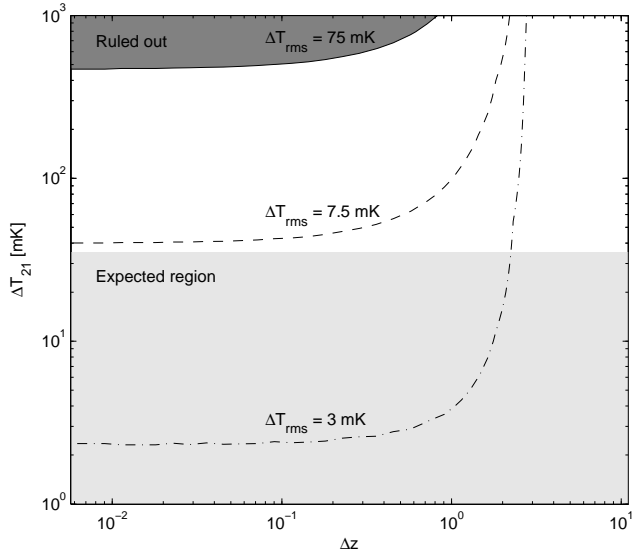


FIG. 6.— Constraints placed by EDGES on the redshifted 21 cm contribution to the sky spectrum. The dark-gray region at the top-left is the portion of the parameter space ruled out by the initial EDGES results with $\Delta T_{rms} = 75$ mK (solid line). The dashed line labelled $\Delta T_{rms} = 7.5$ mK and the dotted line labelled $\Delta T_{rms} = 3$ mK indicated the constraints that could be placed on reionization if the experimental systematics were lowered to the respective values. The light-gray region along the bottom is the general range of parameters believed to be viable. The redshifted 21 cm contribution to the spectrum is modelled according to the description in § 4.1 with $z_r = 8$.

the system down to 50 MHz or lower in order to place constraints on the anticipated transition of the hyperfine line from absorption to emission as the IGM warms before the EOR. Constraining the redshift and intensity of this feature would be very valuable for understanding the heating history of the IGM and, since the transition has the potential to produce a step-like feature in the redshifted 21 cm spectrum with a magnitude over 100 mK (up to a factor of 4 larger than the amplitude of the step during the reionization epoch), it may be easier to identify than the transition from reionization—although the sky noise temperature due to the Galactic synchrotron foreground increases significantly at the lower frequencies, as well. Through these and other global spectrum efforts, the first contribution to cosmic reionization science from measurements of the redshifted 21 cm background will hopefully be achieved in the near future.

This work was supported by the Massachusetts Institute of Technology, School of Science, and by the NSF through grant AST-0457585.

REFERENCES

- Barkana, R., & Loeb, A. 2005, *ApJ*, 626, 1
 Becker, R. H., et al. 2001, *AJ*, 122, 2850
 Benz, A. O., Grigis, P. C., Hungerbühler, V., Meyer, H., Monstein, C., Stuber, B., & Zardet, D. 2005, *A&A*, 442, 767
 Bowman, J. D., et al. 2007, *AJ*, 133, 1505
 Bridle, A. H. 1967, *MNRAS*, 136, 219
 Cen, R. 2003, *ApJ*, 591, 12
 Ciardi, B., & Madau, P. 2003, *ApJ*, 596, 1
 Djorgovski, S. G., Castro, S., Stern, D., & Mahabal, A. A. 2001, *ApJ*, 560, L5
 Fan, X., Narayanan, V. K., Strauss, M. A., White, R. L., Becker, R. H., Pentericci, L., & Rix, H.-W. 2002, *AJ*, 123, 1247
 Fan, X., et al. 2006, *AJ*, 132, 117
 Fan, X., et al. 2003, *AJ*, 125, 1649
 Furlanetto, S. R. 2006, *MNRAS*, 371, 867
 Furlanetto, S. R., Oh, S. P., & Briggs, F. H. 2006, *Phys. Rep.*, 433, 181
 Furlanetto, S. R., Zaldarriaga, M., & Hernquist, L. 2004, *ApJ*, 613, 16
 Gnedin, N. Y., & Shaver, P. A. 2004, *ApJ*, 608, 611
 Haiman, Z., & Holder, G. P. 2003, *ApJ*, 595, 1
 Hogan, C. J., & Rees, M. J. 1979, *MNRAS*, 188, 791
 Iliev, I. T., Scannapieco, E., Martel, H., & Shapiro, P. R. 2003, *MNRAS*, 341, 81
 Iliev, I. T., Shapiro, P. R., Ferrara, A., & Martel, H. 2002, *ApJ*, 572, L123
 Kraus, J. D. 1988, *Antennas* (2nd ed.) (McGraw-Hill Companies)
 Loeb, A., & Zaldarriaga, M. 2004, *Physical Review Letters*, 92, 211301
 Madau, P., Meiksin, A., & Rees, M. J. 1997, *ApJ*, 475, 429
 Madau, P., Rees, M. J., Volonteri, M., Haardt, F., & Oh, S. P. 2004, *ApJ*, 604, 484
 Rohlfs, K., & Wilson, T. L. 1996, *Tools of Radio Astronomy* (Second ed.) (Springer)
 Scott, D., & Rees, M. J. 1990, *MNRAS*, 247, 510
 Shapiro, P. R., Giroux, M. L., & Babul, A. 1994, *ApJ*, 427, 25
 Shaver, P. A., Windhorst, R. A., Madau, P., & de Bruyn, A. G. 1999, *A&A*, 345, 380
 Sokasian, A., Abel, T., Hernquist, L., & Springel, V. 2003, *MNRAS*, 344, 607
 Spergel, D. N., et al. 2007, *ApJS*, 170, 377
 Suh, S. Y., Stutzman, W., Davis, W., Waltho, A., Skeba, K., & Schiffer, J. 2004, *Vehicular Technology Conference, VTC2004-Fall*, IEEE, 1, 225
 Suh, S. Y., Stutzman, W. L., & Davis, W. A. 2003, *Antennas and Propagation Society International Symposium, IEEE*, 2, 156
 Sunyaev, R. A., & Zeldovich, Y. B. 1972, *A&A*, 20, 189
 Tegmark, M., et al. 2006, *Phys. Rev. D*, 74, 123507
 Tozzi, P., Madau, P., Meiksin, A., & Rees, M. J. 2000, *ApJ*, 528, 597
 Wilkinson, A. 1973, *MNRAS*, 163, 147
 Wyithe, J. S. B., & Loeb, A. 2004, *Nature*, 427, 815
 Zaldarriaga, M., Furlanetto, S. R., & Hernquist, L. 2004, *ApJ*, 608, 622
 Zaldarriaga, M., Spergel, D. N., & Seljak, U. 1997, *ApJ*, 488, 1